The Astrophysical Journal, 890:96 (13pp), 2020 February 20 https://doi.org/10.3847/1538-4357/ab6664

Penumbral Brightening Events Observed in AR NOAA 12546

Mariarita Murabito[1], Salvo L. Guglielmino[2], Ilaria Ermolli[1], Marco Stangalini[1,3], and Fabrizio Giorgi[1]
[1] INAF—Osservatorio Astronomico di Roma, Via Frascati, 33, Roma Italy; mariarita.murabito@inaf.it
[2] Dipartimento di Fisica e Astronomia—Sezione Astrofisica, Università degli Studi di Catania, Via S. Sofia 78, I-95123 Catania, Italy
[3] ASI, Agenzia Spaziale Italiana, Via del Politecnico snc, I-00133 Rome, Italy
Received 2019 October 31; revised 2019 December 4; accepted 2019 December 4; published 2020 February 17

Abstract

Penumbral transient brightening events have been attributed to magnetic reconnection episodes occurring in the low corona. We investigated the trigger mechanism of these events in active region NOAA 12546 by using multiwavelength observations obtained with the Interferometric Bidimensional Spectrometer, Solar Dynamics Observatory, the Interface Region Imaging Spectrograph, and the Hinode satellites. We focused on the evolution of an area of the penumbra adjacent to two small-scale emerging flux regions (EFRs), which manifested three brightening events detected from the chromosphere to the corona. Two of these events correspond to B-class flares. The same region showed short-lived moving magnetic features (MMFs) that streamed out from the penumbra. In the photosphere, the EFRs led to small-scale penumbral changes associated with a counter-Evershed flow and to a reconfiguration of the magnetic fields in the moat. The brightening events had one of the footpoints embedded in the penumbra and seemed to result from the distinctive interplay between the preexisting penumbral fields, MMFs, and the EFRs. The IRIS spectra measured therein reveal enhanced temperature and asymmetries in spectral lines, suggestive of event triggering at different heights in the atmosphere caused by the reconnection. The blue asymmetry noted in C II and Mg II h&k lines suggests the occurrence of chromospheric evaporation at the footpoint located in the penumbra as a consequence of the magnetic reconnection process at higher atmospheric heights.

Unified Astronomy Thesaurus concepts: Solar magnetic reconnection (1504); Solar magnetic fields (1503); Active solar chromosphere (1980); Solar photosphere (1518); Solar X-ray emission (1536)

Supporting material: animations

1. Introduction

Present-day high resolution observations reveal the dynamic fine scale structure of sunspots created by magnetoconvective interactions (Borrero & Ichimoto 2011; Rempel & Schlichenmaier 2011). Small-scale features in a sunspot (umbral and penumbral) vary in space and time due to a number of different processes. These include oscillations, waves, jets of plasma, and magnetic reconnection. This is believed to lead to flaring events. The latter phenomena involve plasma heating, particle acceleration, and the release of electromagnetic energy from X-rays to radio wavelengths (Shibata & Magara 2011; Benz 2017).

Smaller-scale energy release phenomena detected over and near sunspot's penumbrae have been related to new magnetic elements in emerging flux regions (EFRs, e.g., Guglielmino 2012; Cheung & Isobe 2014) and to magnetic features moving away from the sunspot toward the boundary of the moat region (moving magnetic features, MMFs), see, e.g., Criscuoli et al. 2012; Li et al. 2019, and references therein), which can cancel with preexisting magnetic fields.

In this regard, Kano et al. (2010) analyzed micro flares around a well-developed sunspot, by using Hinode (Kosugi et al. 2007) satellite data from the X-ray Telescope (XRT; Golub et al. 2007) and the Narrowband Filter Imager mounted on the Solar Optical Telescope (Tsuneta et al. 2008). They found that half of the observed micro flares were caused by magnetic flux cancellation (encounters of opposite polarities in their paper) and when the latter is the main cause, the micro flare has one of the X-ray loops connecting the penumbra to the opposite polarity patch of an EFR or an MMF embedded in the moat.

Recently, Bai et al. (2016) reported on a penumbral transient brightening observed with state-of-the-art instruments installed in the Interface Region Imaging Spectrograph (IRIS; De Pontieu et al. 2014) satellite and the 1.6 m New Solar Telescope (Goode et al. 2010; Goode et al. 2010) at the Big Bear Solar Observatory. This penumbral brightening, whose estimated thermal energy was in the range of nano flares (10^{22}–10^{25} erg), displayed signatures from the chromosphere to the corona. The same authors found that an MMF had appeared close to the penumbral boundary and at the same location of one of the footpoints associated with the observed brightening. Bai et al. (2016) attributed the triggering mechanism of the analyzed event to magnetic reconnection occurring in the low corona and explained the brightening seen in the transition region (TR) and chromosphere as due to the local plasma heated up by downward propagating accelerating particles and thermal conduction. However, due to very weak signals of the observations analyzed, those authors could not find any evidence of the chromospheric evaporation that is expected to follow the heating of the chromospheric plasma from reconnection processes in the low corona. This evaporation has been reported from analysis of large flares (Tian et al. 2014; Graham & Cauzzi 2015), as well as in micro- (Chen & Ding 2010) and nano flares (Testa et al. 2014) observed outside penumbrae. Since the trigger mechanism of the studied brightening could not be clearly identified by their analysis, Bai et al. (2016) solicited more research on the formation process of brightening events observed in penumbral regions.

Indeed, it is well known that the magnetic reconnection can occur on any spatial or temporal scale in the solar atmosphere (Priest & Forbes 2000). Both the current high resolution observations and magnetohydrodynamical (MHD) numerical simulations indicate that interactions of EFRs with preexisting ambient magnetic fields (Archontis 2012; Cheung & Isobe 2014; Schmieder et al. 2014) play a prominent role in models

of large- (e.g., Louis et al. 2015, and references therein) and small-scale eruptive events (e.g., Guglielmino et al. 2010, 2018, 2019, and references therein). In particular, it is expected that the magnetic reconnection can occur at different atmospheric heights depending on the overlying and background magnetic fields and on the strength and size of the EFR (Archontis et al. 2004; MacTaggart et al. 2015). Furthermore, Galsgaard et al. (2005, 2007) demonstrated that the magnetic reconnection strongly depends on the relative orientation between the magnetic components of the emerging flux and the preexisting magnetic field. In fact, only when the two flux systems have almost antiparallel orientation is the magnetic reconnection efficient.

In this study, we analyzed multiwavelength observations of the active region (AR) NOAA 12546 obtained with state-of-the-art instruments to further investigate the trigger mechanism of penumbral brightening events. In particular, we studied the evolution of the penumbral area adjacent to two small-scale EFRs emerged in the AR on 2016 May 20. The analyzed region showed three brightening events detected from the chromosphere to the corona.

The paper is organized as follows: in the next Section we describe the observations and the data processing applied. In Section 3 we feature our analysis and results, which are summarized and discussed in Section 4. Section 5 presents our conclusions.

2. Data and Methods

2.1. Observations

We analyzed high spatial, spectral, and temporal resolution data acquired by the Interferometric Bidimensional Spectrometer (IBIS; Cavallini 2006) at the Dunn Solar Telescope of the National Solar Observatory, the Helioseismic and Magnetic Imager (HMI; Scherrer et al. 2012) and Atmospheric Imaging Assembly (AIA; Lemen et al. 2012) instruments on board the Solar Dynamics Observatory (SDO; Pesnell et al. 2012) satellite, and the IRIS and Hinode/XRT space-borne telescopes.

IBIS observations were carried out on 2016 May 20 when the AR was characterized by a magnetic configuration. The data set consists of full-Stokes measurements taken along the Fe I 617.30 nm and Ca II 854.20 nm lines, each line sampled at 21 spectral positions over a field-of-view (FoV) of about $40'' \times 90''$. The data were acquired with a spectral sampling of 20 and 60 mÅ, and a spatial resolution of 0.16 and 0.23 for the Fe I and Ca II measurements, respectively, with a cadence of 48 s under excellent seeing conditions that lasted about 180 minutes (318 line scans). The data were processed with the methods described by, e.g., Ermolli et al. (2017). The same data set was also analyzed by Stangalini et al. (2018) and Murabito et al. (2019), to which we refer the reader for further details.

SDO data comprise the Space-weather HMI Active Region Patches (Bobra et al. 2014) continuum filtergrams, magnetograms, and Dopplergrams derived from the HMI measurements at the Fe I 617.3 nm line, performed with a resolution of 1″ and a cadence of 12 minutes from 2016 May 19 at 08:00 UT to May 21 at 08:00 UT. Furthermore, we considered AIA filtergrams taken at the 1600, 304, 171, 335, and 131 Å bands (hereafter referred to as A1600, A304, A171, A335, and A131, respectively), with a pixel scale of about 0.6″ and a cadence of 12 s and 24 s for the EUV and UV channels, respectively.

The IRIS data set was acquired at the time of the IBIS measurements on 2016 May 20 from 13:17 UT to 16:30 UT. It consists of a sit-and-stare scan (OBS 3620110063) taken with a cadence of 20 s at the C I 1334.53 Å, Si IV 1402.77 Å, and Mg II h & k 2796.35 and 2803.53 Å lines. Simultaneous slit-jaw filtergrams (SJIs) were acquired in the passbands of the Si IV 1400 Å line and Mg II k line wing (hereafter referred to as I1400 and I2832), with a cadence of 20 s and 97 s, respectively, covering an FoV of $120'' \times 119''$. The I1400 and I2832 data sample plasma at $T = 65{,}000$ K and $T = 6{,}000$–$10{,}000$ K, respectively.

Finally, we analyzed Hinode/XRT images taken through the Al polyimide and the Be thin filters, whose temperature response ranges $6 < \log T < 7.5$ for the former, and has a peak at $\log T = 7$ for the latter (Golub et al. 2007). The two sets of images were acquired with a cadence of 60 s and varying exposure time. These data provide measurements over a FoV of $384'' \times 384''$, with a pixel size of 1.03″. Note that XRT observations were taken simultaneously to IRIS data with some gaps.

2.2. Data Processing

We coaligned IBIS, SDO/HMI, and SDO/AIA observations by applying cross-correlation techniques on cospatial FoVs that were extracted from the three data sets. In particular, we used the first IBIS spectral image taken at the Fe I 617.3 nm line continuum on 2016 May 20 at 13:53 UT as a reference and the corresponding, neighboring-in-time SDO/HMI continuum image and SDO/AIA A1600 filtergram. We employed IDL SolarSoft mapping routines to account for the different pixel size of the data. Since the SDO/AIA data are aligned between them we employed the SDO/AIA A1600 image aligned to the IBIS data as a reference for the remaining SDO/AIA channels. Then, we aligned the IRIS data to the other measurements, by using the IRIS SJIs I2832 filtergrams and the closest in time SDO/HMI continuum images. Finally, we aligned the XRT images using the SDO/AIA A131 filtergrams as an anchor channel. The precision of our data alignment is comparable to the pixel size of the SDO observations, about 0.6″, which is accurate enough for the analysis presented in the following.

To get quantitative estimates of the physical parameters in the analyzed region, we inverted the IBIS data by using the non-LTE inversion code NICOLE (Socas-Navarro et al. 2015). In brief, we assumed five equidistant nodes for temperature, three nodes for each component of the vector magnetic field (B_x, B_y, and B_z), two nodes for the line-of-sight (LOS) velocity, and one node for both the microturbulence and macroturbulence. We performed the inversions in two cycles, by assuming as the starting guess model a modified FALC atmosphere (Fontenla et al. 1993) with a constant value of 1.5 kG for B_z. We refer the reader to the paper by Murabito et al. (2019) for further details.

In order to study the horizontal proper motions and estimate the velocity of the photospheric plasma, we applied the Fourier Local Correlation Tracking technique (FLCT; Fisher & Welsch 2008) to the available SDO/HMI LOS magnetograms. We set the FWHM of the Gaussian tracking window to 15 pixels, in order to follow the collective motions of the

magnetic structures, and made a temporal integration over a time interval of 12 minutes.

In addition, we got pixelwise estimates of the LOS velocity of the photospheric plasma by computing the Doppler shift of the line core of the IBIS Fe I data with respect to the average position of the line core in a quiet Sun region. We computed the line core position by fitting the Stokes I Fe I measurements with a linear background and a Gaussian function.

3. Analysis and Results

From 2016 May 15 to 25, ground-based and space-borne solar telescopes detected the on-disk passage of AR NOAA 12546 (AR hereafter), which emerged in the southern solar hemisphere close to the equator. This AR consisted of a leading, large and almost circular sunspot and a trailing, extended plage region. The sunspot, which was one among the largest such structures observed over the solar cycle 24, kept its regular shape nearly unchanged during the disk passage, while the plage region evolved significantly. The studied sunspot also displayed a large number of MMFs, mostly of type II, i.e., unipolar features with the same polarity of spot (e.g., Zuccarello et al. 2009, and references therein), seen to move almost radially away from the sunspot structure toward the boundary of the moat region.

Both the SDO/HMI and IBIS photospheric observations show that the penumbra of AR was formed by bright filaments and dark spines nearly radially aligned over most of the sunspot structure (Murabito et al. 2019), except for an area close to the EFRs observed on 2016 May 20.

3.1. Magnetic Environment in the Photosphere

Figure 1 shows the region analyzed in our study as deduced from SDO/HMI continuum observation performed on 2016 May 19 at 13:34 UT and the region of interest (ROI) discussed in the following and shown in Figures 3, 6, and 7. The bottom panel of Figure 1 displays the LOS magnetogram with overplotted horizontal velocity.

Starting from 2016 May 19 12:00 UT the ROI showed in about 24 hr an increase of the LOS magnetic flux of about $(2–4) \times 10^{20}$ Mx for the positive and negative polarity, and a flux decrease afterwards. This flux variation, which is reported in Figure 2, followed the evolution of the region summarized in the panels of Figure 3, which show maps from SDO/HMI observations at 9 representative times from 2016 May 19 08:00 UT to May 21 00:00 UT.

On 2016 May 19 08:00 UT the ROI only included the southern sector of the penumbra and moat area nearby (Figure 3, first row). A few hours later, at 16:00 UT, negative polarity patches (labeled N in Figure 3, panel (b2)) from the new flux of an EFR emerging at X = [20 , 50], Y = [15 , 40], had already merged with preexisting network field forming a small pore and a few fainter structures (labeled N_1 and N_2 in Figure 3, panel (b3)). These structures also received the negative polarity flux from a second EFR appearing on 2016 May 20 01:00 UT. Thereafter, positive polarity patches streaming out from the penumbra and from the second EFR merged to form small-scale structures in the southeast section of the ROI (at X = [5 , 30], Y = [10 , 25]) that later on, e.g., at 13:48 UT, were only merely discernible.

During the emergence of the second EFR, a bright lane (marked with red arrows in Figure 3, panels (a4)–(a5)) and a few dark patches (marked with the orange arrow in Figure 3, panel (a6)) appeared in the penumbra near the EFR, by creating a gap in the structure (see green arrows in Figure 3, panels (a4)–(a6)) that separated filaments with different orientation.

Later, the filaments closer to N_2 (black oval in Figure 3, panels (b7)–(b8)) broke away from the penumbra (black oval in Figure 3, panel (b8)) when the small-scale negative flux patches from the two EFRs and preexisting fields coalesced and got more aggregated (N_3 in Figure 3, panels (b7)–(b9)).

The animated version in Figure 3 (panels (a) and (b)), available in the online material clearly shows the entire

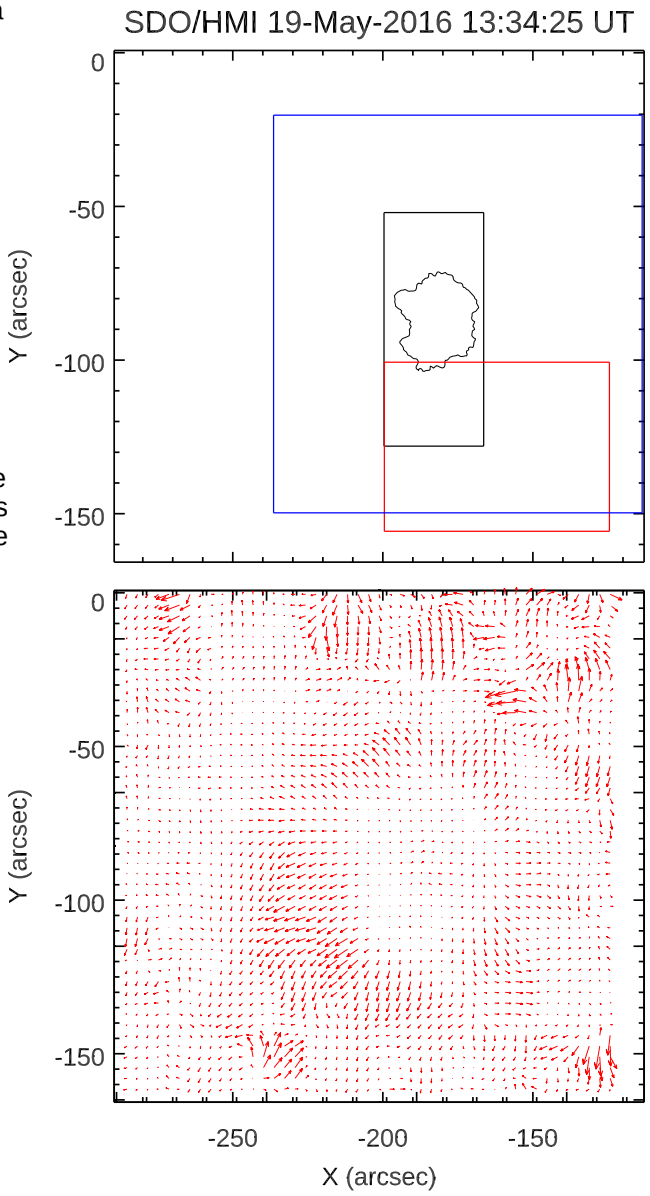

Figure 1. Subarray extracted from the full-disk continuum intensitygram (top panel) and LOS magnetogram (bottom panel) taken by SDO/HMI on May 19 at 13:34 UT and centered on the studied AR. Values of the LOS component of the magnetic field are saturated at ±500 G. The black and blue boxes indicate the FoV of the IBIS and IRIS observations analyzed in our study, respectively, while the red box shows the ROI where the studied brightening events occur. Here and in the following figures, solar north is to the top, and west is to the right. The horizontal velocity estimated with FLCT is overplotted on the LOS magnetogram. The white reference arrow indicates a horizontal velocity of plasma of 1 km s^{-1}. See Sections 2 and 3 for more details.

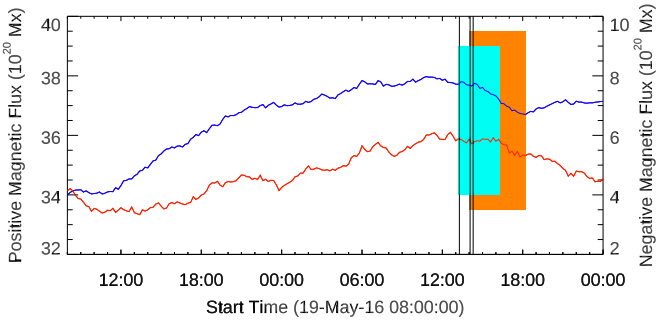

evolution described above and the diverse MMFs discussed below.

The penumbra had a rather homogeneous structure with inclination of about 60°–90° (Figure 3, third column), except for a few elongated patches with inclination in the range 40°–60° (marked with the white oval in Figure 3, panels (c3)–(c7)) in the area that broke away. These features were clearly linked to the positive polarity patches of the EFR. The region also displayed two systematic flow patterns, which are shown in Figure 3 (fourth column). The former, directed toward the first EFR, led to the formation of N_3 by the merging of N_1 and N_2, while the second southern-ward pattern contributed to the evolution of the small-scale positive polarity features. Note that the emergence of both EFRs was characterized by strong shear motions with values of the horizontal velocity of the plasma of about 1 km s^{-1}.

The IBIS data provide a close-up view of the evolution of the ROI and of the physical properties therein. In particular, we show in Figure 4 the analyzed area from the IBIS observations taken on 2016 May 20 at 14:00 UT (left panels) and 17:00 UT (right panels), along with results from their inversion. The IBIS data at 14:00 UT indicate that the bright gap in the penumbra (yellow oval) already noticed in the SDO/HMI observations separates filaments with different orientation in the irregularly shaped penumbral sector. The dark structures (red arrow), whose length was of about 10″, decreased in size over time until they were no longer detected, e.g., on 2016 May 20 at 18:00 UT. Noticeably, the plasma LOS velocity in small-scale patches of these structures was opposite with respect to the regular Evershedows nearby (Figure 4 panel (c)).

Figure 4 (panels (d)–(e)) also displays filaments at the atmospheric height $\log\tau = -1.0$ with average values of the field strength and inclination of about 1.4 kG and about 45°, respectively, in the area that broke away from the penumbra compared to the values for the same quantities of 0.9 kG and 80° for the homogeneous filaments nearby. Later, e.g., at 17:00 UT, the field pattern in the region was unchanged but for the slightly larger extension of the inhomogeneous patches.

3.2. Signatures from the Chromosphere to the Corona

At the chromospheric heights sampled by the IBIS Ca II 854.2 nm measurements, the ROI showed a bundle of filaments with intense and repeated brightening at various locations, especially in the area of the two EFRs. These small-scale enhancements were observed in the form of either circular or elongated features (see the online animation of the Ca II line core images in Figure 4). Moreover, at $\log\tau = -4.6$ (Figure 4, panels (f)–(g)) the ROI exhibited average values of the field strength of about 0.9 kG and field inclination ranging from 60° to 100°, except for some small-scale patches in the inhomogeneous area with field inclination lower than 40°.

The transients observed in IBIS Ca II data were also manifested in the evolution of the average intensity measured over the ROI in the IRIS 1400, SDO/AIA, and Hinode/XRT observations. Figure 5 compares the light curves derived from the above data for the time interval of simultaneous IBIS and IRIS data, along with the variation of the X-ray flux measured by the GOES-15 satellite (Bornmann et al. 1996).

All the light curves shown in Figure 5 display a couple of remarkable intensity increases standing out with respect to long-term and smooth variations. In particular, we considered the three abrupt intensity changes marked with vertical dashed lines in Figure 5 and referred to in the following as E1, E2, and E3. Two of these peaks, specifically E2 and E3, had clear counterparts in the variation of the X-ray flux measured by GOES-15 (red curve in Figure 5) and correspond to B-class flares. The above intensity increases, which lasted a few minutes for all the considered data, had different amplitudes depending on the event and wavelength, see, e.g., the peak value for the E2 and E3 events.

In an attempt to localize the source regions and to investigate the possible trigger mechanisms of the above events, Figure 6 displays SDO/HMI, SDO/AIA, and IRIS data taken over the time interval considered in Figure 5. The various panels in Figure 6 show brightening events whose footpoints and emission contours are overplotted on the I2832 observations for ease of comparison. We clearly noticed two homologous small-scale flaring events developed over a sigmoidal region (panels in the first and third rows of Figure 6). These events correspond to E1 occurring at 13:27 UT and E3 recorded by GOES-15 as B-class flares at 14:32 UT, about one hour later than E1. The eastern footpoint of the flaring region was lying in the penumbra, while the other was close to the patch of negative polarity flux N_1. It is worth noting that the latter footpoint can be easily identified in most of the SDO/AIA coronal observations that also show an intensity enhancement in the central part of the sigmoidal flaring area during E3. The latter area is only faintly detected in cotemporal chromosphere and TR, see, e.g., I1400 and A304 maps.

Between the above homologous flaring events, we observed the occurrence of E2, a small-scale brightening appeared at about 14:08 UT in the left side of the ROI (panels in the second row of Figure 6) in the form of three elongated small-scale features seen in the A304 and A131 data, and only partly detected in I1400 observations. These bright patches were clearly aligned to penumbral filaments and cospatial to the small-scale positive flux features described in Section 3.1.

We further investigated the differences among E1, E2, and E3 by using I1400 observations, some examples of which are shown in Figure 7. The evolution of E1 was fast (Figure 7, top panels) and with simultaneous signatures seen in the light curves and observations of I1400, A131, and A304. The E2 event lasted about 7 minutes and reached its maximum extension 3 minutes after its start (Figure 7, middle panels) in the form of a bright knot appeared in the penumbra. Three minutes after the first appearance of the bright knot, a thin bright flame connected it to a small bright patch outside the